



Article

Study on the Formation of Reactive Material Shaped Charge Jet by Trans-Scale Discretization Method

Guancheng Lu ¹, Chao Ge ¹, Zhenyang Liu ¹, Le Tang ² and Haifu Wang ^{1,*}

¹ State Key Laboratory of Explosion Science and Technology, Beijing Institute of Technology, Beijing 100811, China; 3120195177@bit.edu.cn (G.L.); gechao@bit.edu.cn (C.G.); 3120215137@bit.edu.cn (Z.L.)

² Beijing Institute of Space Launch Technology, Beijing 100076, China; letang.cn@gmail.com

* Correspondence: wanghf@bit.edu.cn

Abstract: The formation process of reactive materials shaped charge is investigated by X-ray photographs and numerical simulation. In order to study the formation process, a trans-scale discretization method is proposed. A two-dimensional finite element model of shaped charge and reactive material liner is established and the jet formation process, granule size difference induced particle dispersion and granule distribution induced jet particle distribution are analyzed based on Autodyn-2D platform and Euler solver. The result shows that, under shock loading of shaped charge, the Al particle content decreases from the end to the tip of the jet, and increases as the particle size decreases. Besides, the quantity of Al particles at the bottom part of the liner has more prominent influence on the jet head density than that in the other parts, and the Al particle content in the high-speed section of jet shows inversely proportional relationship to the ratio of the particle quantity in the top area to that in the bottom area of liner.



Citation: Lu, G.; Ge, C.; Liu, Z.; Tang, L.; Wang, H. Study on the Formation of Reactive Material Shaped Charge Jet by Trans-Scale Discretization Method. *Crystals* **2022**, *12*, 107. <https://doi.org/10.3390/cryst12010107>

Academic Editors: Yong He, Wenhui Tang, Shuhai Zhang, Yuanfeng Zheng, Chuanting Wang, Francesco Stellato and Artem Pronin

Received: 11 November 2021

Accepted: 6 January 2022

Published: 14 January 2022

Publisher's Note: MDPI stays neutral with regard to jurisdictional claims in published maps and institutional affiliations.



Copyright: © 2022 by the authors. Licensee MDPI, Basel, Switzerland. This article is an open access article distributed under the terms and conditions of the Creative Commons Attribution (CC BY) license (<https://creativecommons.org/licenses/by/4.0/>).

Keywords: reactive material; shaped charge jet; trans-scale discretization; formation

1. Introduction

Reactive material, fabricated by pressing/sintering fluoropolymer and active metal powders, characterized by its metal-like strength and impact-initiated energy release, has been widely researched since 2000s [1–3]. The reactive jet, generated by shaped charge with reactive material liner, causing catastrophic damage to the armor due to its penetration and internal explosion properties [4], provides a novel application of reactive material and has received dramatically raised concern in recent years [4].

The present researches on reactive material jets involve jet formation [5], penetration capability [6], energy release characteristics [7], as well as the enhanced terminal effect [8,9]. Experimental and numerical methods, such as shock loading experiments by shaped charge [10], X-ray photographs investigation [5], and macroscopic modeling [11] are general methods applied to study the formation process and terminal effects of reactive material jets.

The reactive liner forms a jet in an extremely short duration. Apart from this, the reactive material jet would undergo an initiation and explosion process during its formation. Although numerical simulation has been widely used to investigate this issue, the reactive material was generally set to be homogeneous without regarding the granular metal particles. Recently, mesoscopic simulation on composite materials impacted by dynamic loading has gained much progress [12,13]. Researchers propose a two-dimensional real microstructure-based modeling technology to describe reactive material in much smaller scale [14], and appropriate equation of state parameters are given [15]. Mesoscopic numerical simulation is also introduced into the study of metal composites jets formation [16,17], while previous work [18,19] has also demonstrated the feasibility of the mesoscale simulation method for the PTFE-Al granular composites. Besides, the previous study also presented the damage enhancement behavior for typical PTFE-Al reactive material liner [11]

and double-layered liner shaped charges [10], and reveals that the jet density and material ratio have great influence on damage ability using macroscopic modeling. However, the jet formation process of reactive material liner under shock loading, regarding the mesoscale material characteristics, evolution of structures, and effect on terminal damage, are of great complexity, and are not reported so far.

In this research, a trans-scale discretization method is proposed. Two-dimensional finite element model of shaped charge and reactive material liner is established. Additionally, the validity of the trans-scale numerical simulations method is proved by the photographs of the X-ray experiment. Based on Autodyn-2D platform and Euler solver, the jet formation process, granule size difference induced particle dispersion, and granule distribution induced jet particle distribution are studied. The results would provide a valuable guide for the design and application of reactive material liner and shape charge.

2. Experiment Setup and Simulation Method

2.1. Experiment Setup

In this research, a typical shaped charge structure with a mono-cone reactive material liner is presented to study the influence of mesoscopic reactive material characteristics on the jet formation process. The warhead, depicted in Figure 1, mainly consists of an explosive and a mono-cone reactive material liner. The high explosive 8701 is poured into the press mold and a pressure load of 200 MPa is applied at room temperature, thus the diameter and length of the charge are both 40 mm, while the density of the charge is 1.71 g/cm^3 . The cone angle and thickness of the liner are 60° and 4 mm, respectively. Detonation point is located at the center of the bottom of the charge.

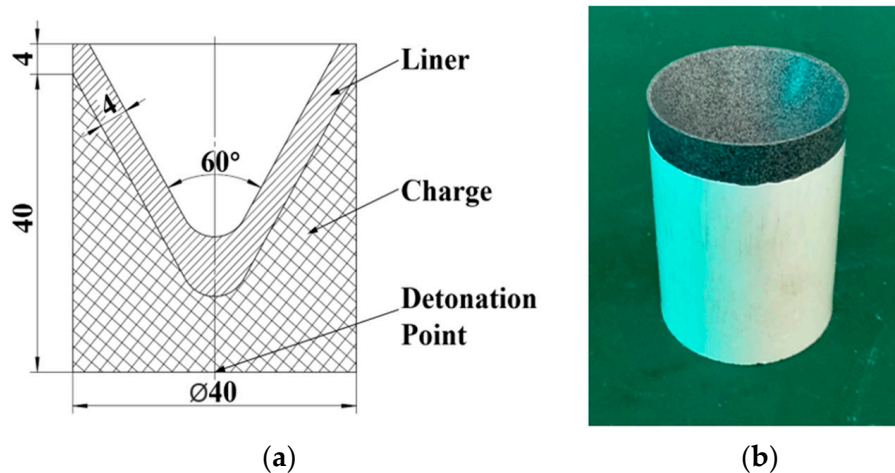


Figure 1. Structure and photograph of shaped charge for X-ray experiment: (a) structure and (b) photograph.

The PTFE/Al (70 wt.%/30 wt.%) reactive material liners are prepared by typical mixing/pressing/sintering method. Firstly, Al particles with an average diameter of $70 \mu\text{m}$ are dried and uniformly mixed with the PTFE matrix. Component mixtures are then pressed via a mold to shape a liner structure with particularly designed geometrical characteristics. Finally, the pressed liner would undergo a sintering cycle to further improve the mechanical and chemical properties.

The schematic diagram of the experimental setup is shown in Figure 2a, and the corresponding photograph is shown in Figure 2b. As can be seen, the warhead is positioned on a standoff (an experiment device), and an X-ray system is used to capture the formation of the reactive material jet. In the testing process, the two X-ray tubes were placed in different positions at the same distance from the negative, and the two rays intersected with the axis of the shaped charge at a certain angle. According to the prior simulation estimation, the times of jet head reaching 1 CD (charge diameter) standoff (the distance

between the jet head and the initial position of the liner bottom) and 2 CD standoff were obtained. It should be noted that, since the damage effect of the reactive material jet is greatly influenced by the standoff, and the optimum standoff of reactive material jet is about 1 CD–2 CD [20], thus the times corresponding to these two standoffs are selected. The two different times were then set for the two ray tubes as ray emission delay times, where the initial time corresponds to the moment of the detonator being initiated. Thus, two appearances of the jet at different times were obtained on the negative films. The protective plate is also used to prevent the jet from impacting the cement floor.

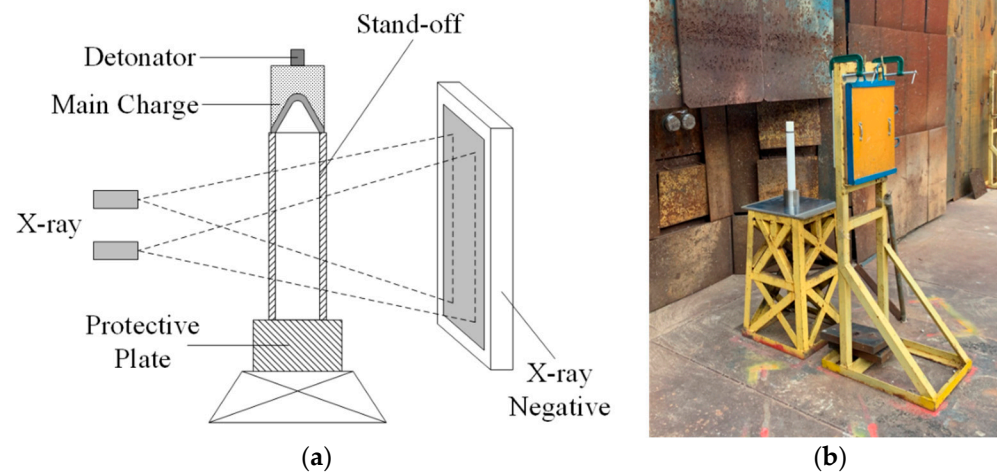


Figure 2. Experimental principle and setup of X-ray: (a) experiment principle and (b) setup of X-ray.

2.2. Trans-Scale Discretization Model

On this basis of the above mixing/pressing/sintering process of the reactive material liner, the Al particles could be assumed to have ideal roundness with diameters conforming to the lognormal hypothesis, and their positions are random without overlap, and the particle diameter and initial distribution are used respectively as control groups.

Therefore, the major issue of developing the discretization model is to fill the Al particles randomly into polymer matrix liner. The generation method of random circular particles is developed using Python programming and includes the following steps:

- (1) Calculate the liner area A_{liner} , then the total Al particle area A_{Al} can be obtained from:

$$A_{Al} = \frac{W_{Al}}{\rho_{Al} \cdot \left(\frac{W_{Al}}{\rho_{Al}} + \frac{1-W_{Al}}{\rho_{PTFE}} \right)} A_{liner} \quad (1)$$

where ρ_{Al} and ρ_{PTFE} is the density of Al and PTFE respectively, and W_{Al} is the mass fraction of aluminum particles.

- (2) Obtain a random particle diameter according to the lognormal distribution of Al particle diameter with consideration of the mean and standard deviation [14]. In this paper, the standard deviation of random particle diameters in all cases are set as 10% average particle diameter, and typical distribution of aluminum particle diameters is shown in Figure 3.
- (3) Generate a random particle coordinate (x, y) in the liner region, and regenerate another one if the edge of the particle exceeds the liner boundary or the particle overlaps with the existing particles.
- (4) Repeat steps 2 and 3 until the Al particle area meets the following condition:

$$\sum_{i=1}^n \pi R_i^2 \geq A_{Al} \quad (2)$$

where R_i represents the radius of each Al particle.

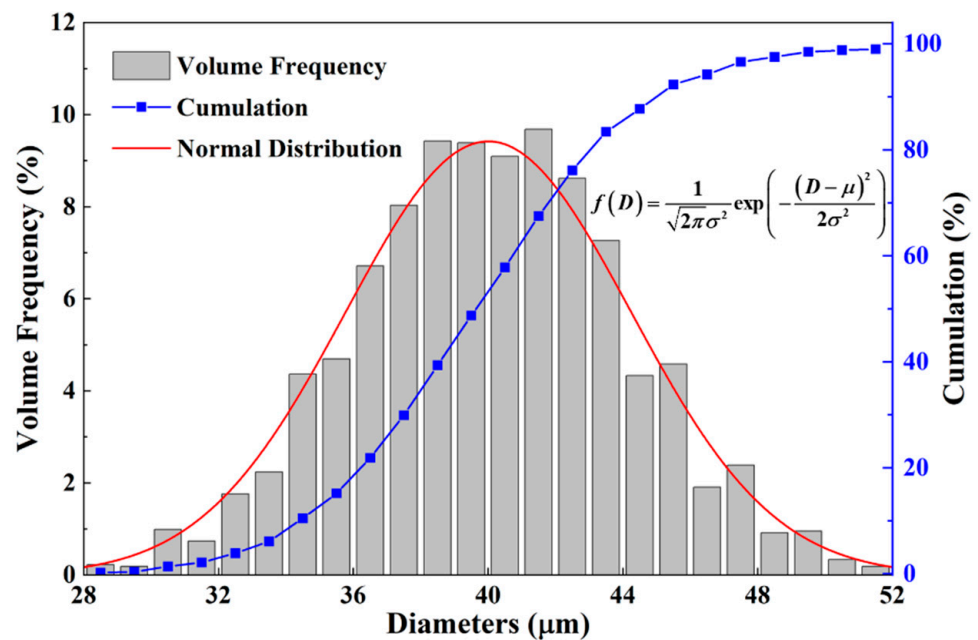


Figure 3. Distribution of aluminum particle diameters.

Finally, the discretization model of typical PTFE-Al liner could be obtained, as described in Figure 4. The diameters and coordinates of all the particles are finally converted into node data information for further characterization.

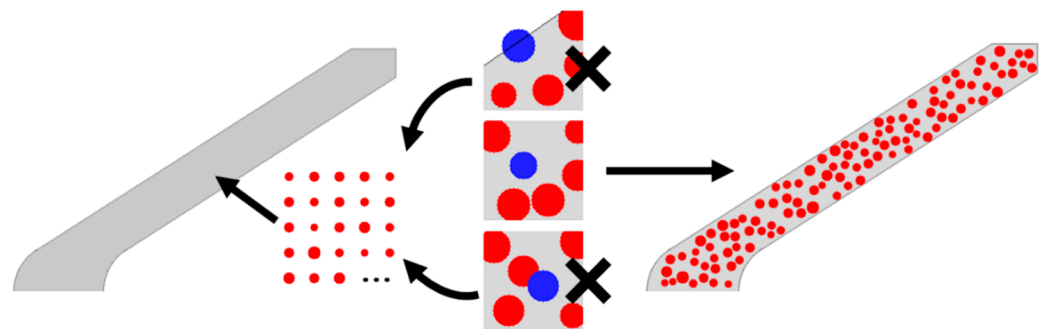


Figure 4. Generation process of typical PTFE-Al liner discretization model.

2.3. Finite Element Model

The finite element models are developed using Euler solver based on the Autodyn-2D platform. As shown in Figure 5, the model consists of a bigger air part (9 mm × 3.5 mm) joined with a smaller one (4 mm × 1.5 mm), which aims to shorten the computation duration. However, meshing is quite difficult because on one hand, fewer nodes lead to lower resolution and loss of accuracy, thereby losing information at the interface between matrix and particles; on the other hand, the number of nodes cannot be excessive due to computing power limitations. Therefore, considering that the average diameter of the Al particles is 40–100 μm, the two-dimensional axisymmetric numerical models are developed with a mesh size of 5 μm × 5 μm. Lastly, the flow-out (ALL EQUAL) boundary is set to eliminate the boundary effect.

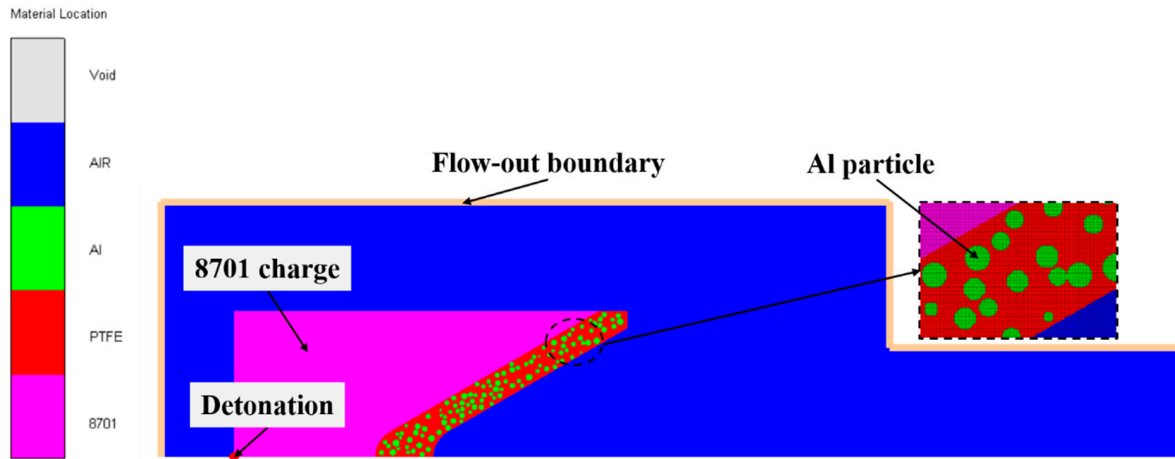


Figure 5. 2D finite element model of the PTFE/Al liner shaped charge.

In this paper, the expansion of the detonation product for 8701 explosive is described by the JWL equation of state (EOS), according to the following form:

$$P = A \left(1 - \frac{\omega}{R_1 V} \right) e^{-R_1 V} + B \left(1 - \frac{\omega}{R_2 V} \right) e^{-R_2 V} + \frac{\omega E_0}{V} \quad (3)$$

where A , B , R_1 , R_2 , and ω are material constants, E_0 represents the detonation energy per unit volume, and V is the relative volume. The corresponding parameters of 8701 explosive are from reference [6], in which $\rho_0 = 1.71 \text{ g/cm}^3$, $A = 524.23 \text{ GPa}$, $B = 7.678 \text{ GPa}$, $R_1 = 4.2$, $R_2 = 1.1$, $\omega = 0.34$, $E_0 = 8.499 \text{ GPa}$, CJ detonation pressure $P_{CJ} = 28.6 \text{ GPa}$, and detonation velocity $D = 8315 \text{ m/s}$.

The shock EOS is used to describe the behavior of Al and PTFE matrix. In the Autodyn-2D program, the shock EOS is established from the Mie–Gruneisen form of EOS based on shock Hugoniot,

$$P = P_H + \Gamma \rho (E - E_H) \quad (4)$$

where it is assumed that $\Gamma \rho = \Gamma_0 \rho_0 = \text{constant}$ and

$$P_H = \frac{\rho_0 c_0 u (1 + u)}{(1 - (s - 1)u^2)} \quad (5)$$

$$E_H = \frac{1}{2} \frac{P_H}{\rho_0} \left(\frac{u}{1 + u} \right) \quad (6)$$

where Γ_0 is the Gruneisen coefficient, $u = (\rho/\rho_0) - 1$, ρ is the current density, ρ_0 is the initial density, s is a linear Hugoniot slope coefficient, and c_0 is the bulk sound speed. The Johnson–Cook strength model, which combines the strain hardening, strain rate strengthening, and temperature softening effect, is used to represent the strength behavior of Al particles and PTFE matrix. The model defines the yield stress σ as:

$$\sigma = (A + B(\bar{\epsilon}^p)^n) \left(1 + C \ln \dot{\epsilon}^* \right) (1 - T^{*m}) \quad (7)$$

where $\bar{\epsilon}^p$ is the effective plastic strain, $\dot{\epsilon}^* = \dot{\epsilon}/\dot{\epsilon}_0$ is the normalized effective plastic strain rate for $\dot{\epsilon}^* = 1.0 \text{ s}^{-1}$, T^{*m} is the homologous temperature, where $T^{*m} = (T - T_{room}) / (T_{melt} - T_{room})$, and A , B , C , n , and m are material constants. Detailed material parameters of the Al and PTFE are listed in Tables 1 and 2 [15].

Table 1. EOS parameters of the materials.

Material	ρ_0 (g/cm ³)	c_0 (m/s)	s (–)	γ_0
Al	2.71	5250	1.370	2.00
PTFE	2.15	1680	1.123	0.59

Table 2. Strength parameters of the materials.

Material	A (MPa)	B (MPa)	C	m	n	T_m (K)
Al	265	426	0.015	1.00	0.34	775
PTFE	11	44	0.120	1.00	1.00	350

2.4. Treatment of Mixed Material Grid

After calculation based on the finite element model, the PRT history file containing all grid data for each selected time is obtained through the print function of Autodyn software, then the data is analyzed using Python programming. However, in the Euler solver, multiple materials are mapped onto the Euler grid through a volume fraction technique [21], while all variables are grid centered. This characteristic leads to the appearance of the mixed material grids, which affects the tracking and calculation of the material distribution. Thus, the mixed grid is transformed into a specific material element according to the following method:

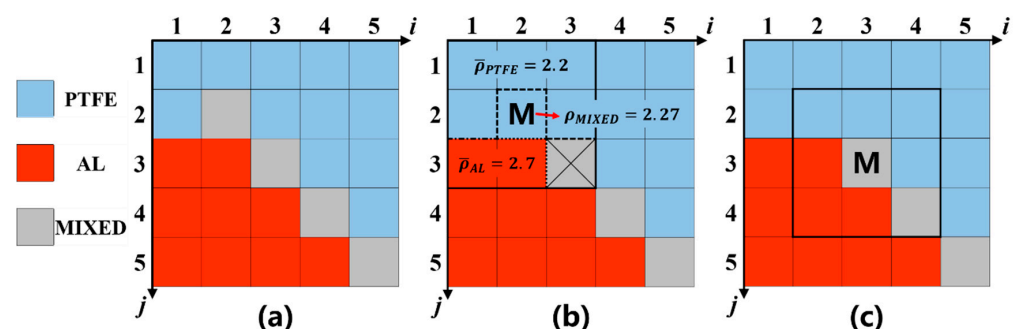
- (1) According to the data of 8 grids around the hybrid grid, the average density of the same material grid except the mixed ones is calculated respectively:

$$\rho_{material,i} = \frac{\sum_1^n \rho_{unit,n}}{n} \quad (8)$$

where $\rho_{material,i}$ represents the average density of each substance in the surrounding grids, $\rho_{unit,n}$ is the density of a unit corresponding to the substance, and n is the total number of the units of this material.

- (2) The material of the target grid is replaced by the surrounding material whose average density is closest to the target one.

For example, as shown in Figure 6, the typical partial material grid graphic (Figure 6a) consists of the PTFE/Al/mixed grids. Following the order from top to bottom and from left to right, the mixed grid ($i = 2, j = 2$) is processed first. According to the above method, the mixed grid ($i = 3, j = 3$) is ignored, only the density of the other five PTFE grids and two Al grids is considered (Figure 6b). Due to the density of the mixed grid ($i = 2, j = 2$) is closer to the average density of PTFE, the material of the mixed grid ($i = 2, j = 2$) is transferred into PTFE. Repeat these steps (Figure 6c) to continue processing the mixed grid ($i = 3, j = 3$) until all the grids are searched. Finally, all the mixed material grids are converted into specific material grids, and then all the grid data can be analyzed by Python programming.

**Figure 6.** The processing method of the mixed material grids: (a) initial grids, (b) treatment of mixed material grid ($i = 2, j = 2$) and (c) repeat the treatment for next mixed material grid ($i = 3, j = 3$).

3. Result and Discussion

3.1. Comparison between Experimental and Simulated Results

The comparison between the experimental and simulated results is presented in Figure 7. The exposure times of the two X-ray pictures are $16\ \mu\text{s}$ and $21\ \mu\text{s}$, corresponding to the situation when the jet tip reaches 1 CD and 2 CD standoff, respectively. It can be seen from the X-ray that the jet is constantly elongated in the forming process, and the morphology shape of the jet is clear when it reaches 1 CD standoff. At the 2 CD standoff situation, the tip and neck of the jet are not very clear, though the shape and contour of the jet still exist. That may indicate that some materials react at the tip of the jet though the overall shape of the jet is relatively stable at a 2 CD standoff.

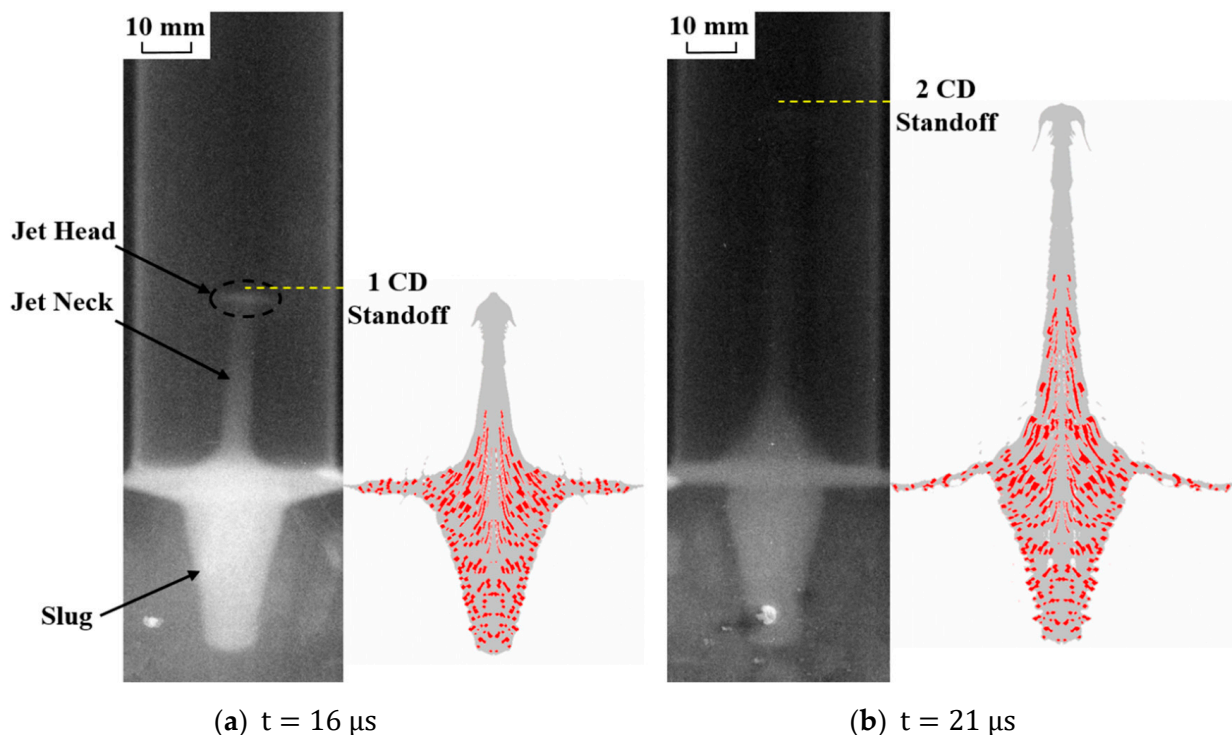


Figure 7. Comparison between experimental and simulated results.

At the same time, the morphologies of the reactive material jet formation process shown in the X-ray photographs agree well with the numerical simulation results. In the simulation image, the red part represents Al and the gray part represents the PTFE matrix, respectively. By comparison, it can be found that when the standoff is 1 CD, the head and neck of the jet in the X-ray photo are clearer than the slug, while the Al particles in the jet head and neck are less than the part of the slug in the simulation. It indicates that low content of Al particles in the jet (low material density) would reduce the clarity of the X-ray image. When the standoff is 2 CD, the part with more Al particles in the simulation also has higher definition in the X-ray film. At the same time, compare the two X-ray images, the 1 CD standoff film is brighter than the 2 CD one. That is most likely because the materials in the jet are more diffuse in the 2 CD situation, which leads to lower density than the 1 CD jet, thus the brightness on the 2 CD picture is darker. On the other hand, in the 2 CD standoff case, some materials may react, thus reducing the brightness of the picture. However, according to reference [6], the average initiation delay time is about $120\ \mu\text{s}$, thus the reaction of the reactive materials at $21\ \mu\text{s}$ is not the main reason for the darker X-ray image. Therefore, it is necessary to analyze the dispersion characteristics of Al particles in the jet forming process for further analysis of the penetration and reaction performance of the reactive material jet.

3.2. Formation of Reactive Material Jet

Figure 8 shows the formation process of a typical reactive material jet. After explosion of the main charge, the reactive material liner is integrally accelerated by the shock wave and detonation products. At 5 μs and 10 μs , the inner wall of the liner collapses and gathers into the symmetry axis to form the jet due to its relatively higher speed. Because of the lower density, the PTFE in the liner accelerates faster and becomes the main component of the jet. With the increase of time, the jet containing both PTFE and Al gradually elongates, but the content of PTFE in the jet is significantly higher than that of Al.

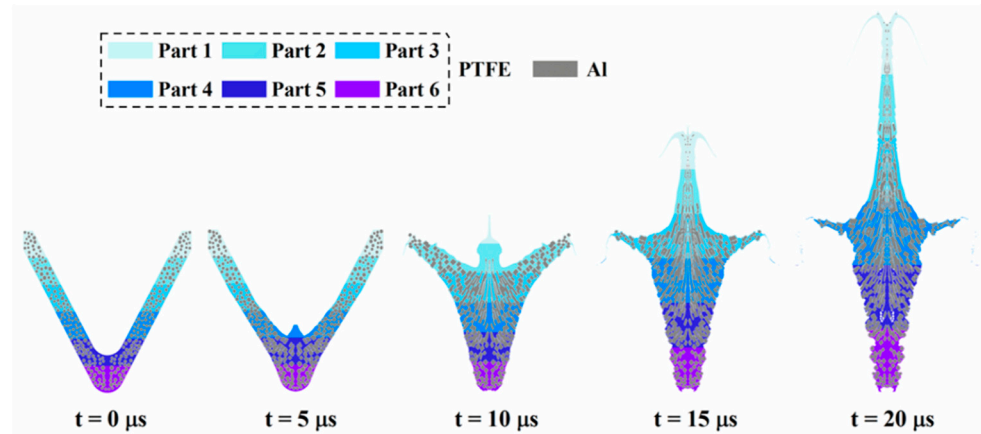


Figure 8. Formation of typical reactive material jet.

To investigate the velocity difference between PTFE and Al during the forming process, the liner and jet in Figure 8 are divided into six equal-length parts. The curves of the velocity difference between the two components from part 2 to part 6 over time are shown in Figure 9a. Since the jet head is composed of PTFE with a higher relative velocity, from 5 μs to 10 μs , there is a period of time during the jet forming process when the jet head (part 1 when $t = 10 \mu\text{s}$ in Figure 8) has no Al particles. Thus, the velocity difference in part 1 corresponding to the tip area of the jet is not steady and the data is not included in Figure 9a. The average velocities of Al and PTFE in the reactive material jet at different times are shown in Figure 9b.

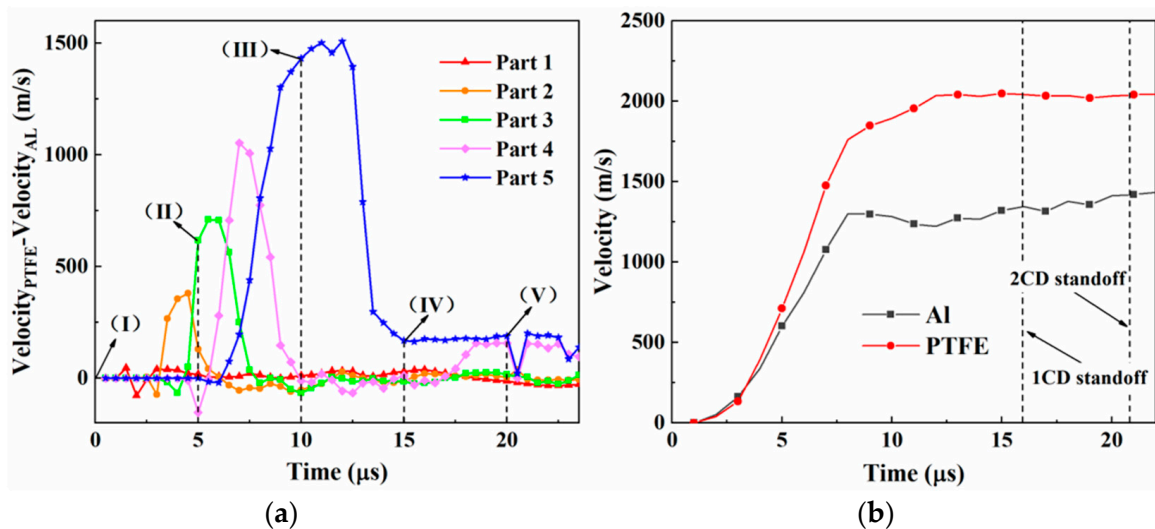


Figure 9. Velocity–time curve of the Al and PTFE in the reactive material jet: (a) the velocity difference between PTFE and Al of each part versus time; (b) the velocity of total Al and PTFE versus time.

Overall, the velocity of Al and PTFE increases simultaneously at the initial acceleration process. However, after 5 μs , the PTFE accelerates faster, up to about 2000 m/s, while the velocity of Al increases more slowly to 1500 m/s. This may be the difference between the density of the two components that contributes to the different particle velocities under the same impact load. However, the two components cannot transfer their stress stably due to the extremely short period of the jet formation process. Therefore, the relative displacement of the two components appears and finally forms the density gradient along the axis of the jet.

For the different parts, the velocity difference curves reach the peak in sequence from part 6 to part 2. It suggests that as the liner collapses, the two components are accelerated and form relative displacement. For each part, the PTFE component moves faster than Al particles, and thus flows forward relative to the Al particles. At the same time, the velocity of the part closer to the jet head is much higher than the backward parts, leading to a larger velocity difference and relative displacement. Finally, fewer aluminum particles remain in the part with higher velocity.

In Figure 10, the reactive material jet at a standoff of 2 CD is equidistantly divided into 10 parts and the Al particle mass fraction of each part is shown in the calculated Al content curve. The result shows that the Al particle content gradually decreases along the symmetry axis from the slug to the jet tip, which corresponds with the previous statement about the gradient density.

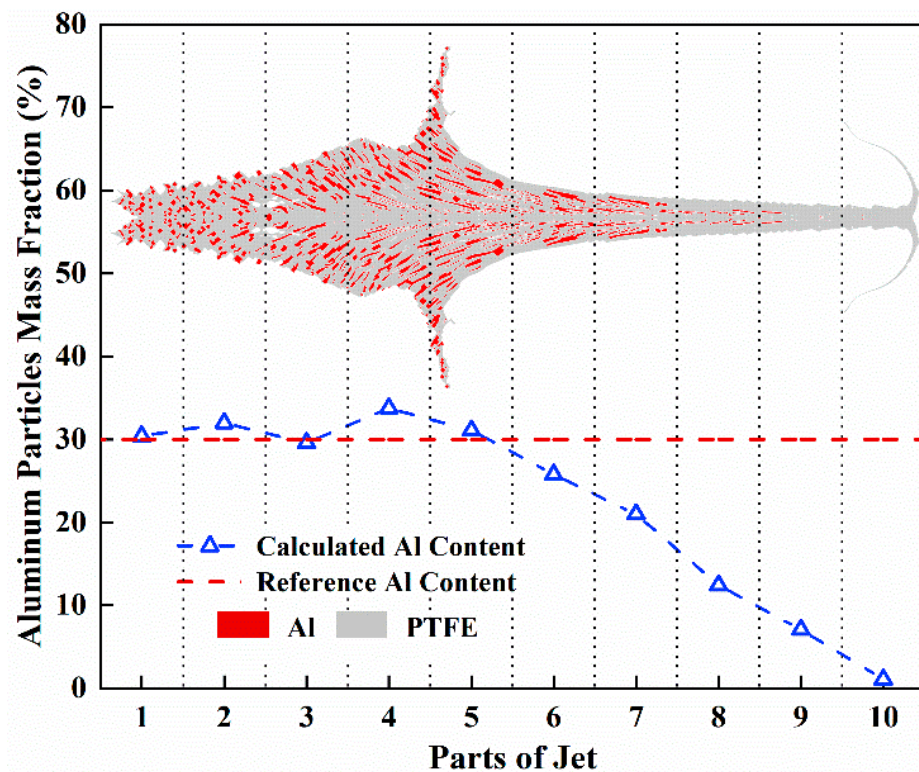


Figure 10. Aluminum particles mass distribution along the jet axis at 2 CD standoff.

3.3. Granule Size Difference Induced Particle Dispersion

In order to study the influence of the granule size on the particle distribution characteristics of the reactive material jet, four granule sizes (40 μm , 60 μm , 80 μm , and 100 μm) are chosen to build the discrete models. At the same time, to distinguish the different parts of the jet, the threshold velocity is defined as 2000 m/s in this article to divide the jet into a high-speed section (HSSJ) and a low-speed section (slug). As shown in Figure 11a, the velocities of all the materials (include Al and PTFE) in HSSJ are over 2000 m/s. Besides, Figure 11b shows the parts whose velocities are over 2000 m/s and below 2000 m/s in the

jets of different standoffs, and the region shape of HSSJ in all standoff cases are basically the same except for stretching over time.

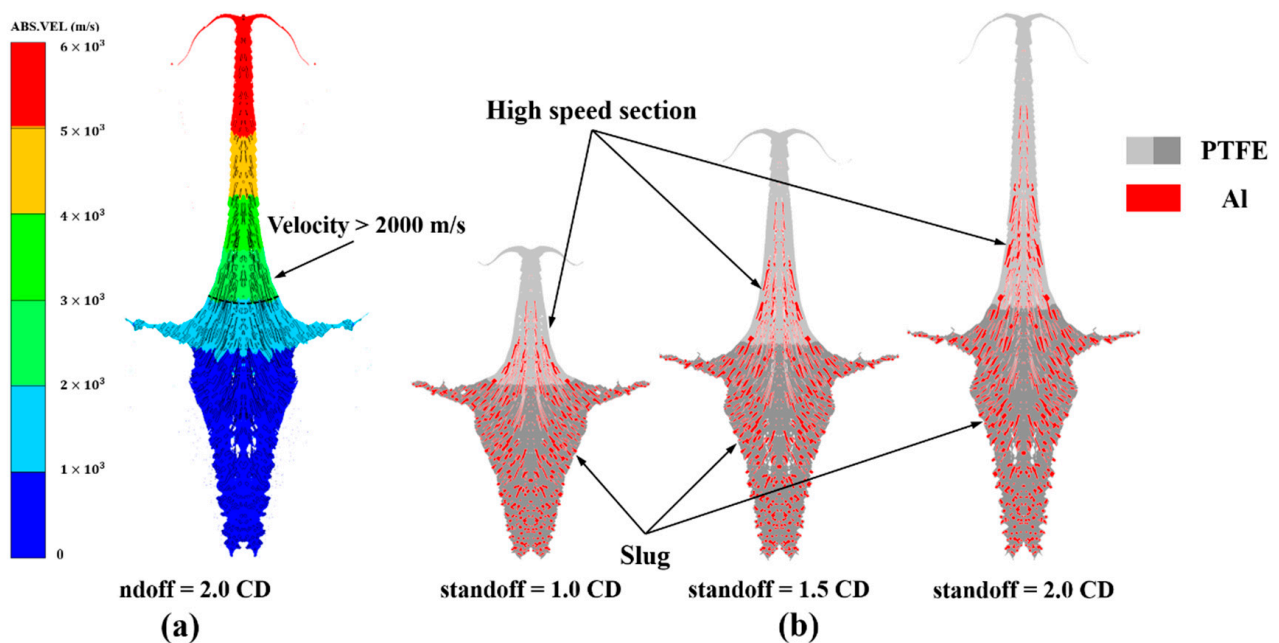


Figure 11. The velocity profile and region division of jets: (a) velocity profile of 2 CD-standoff jet; (b) the HSSJ and slug of different standoffs.

The aluminum content in the HSSJ is analyzed for different granule sizes, at different standoff values. The results are shown in Table 3. The data in Table 3 illustrates that the particle content of the HSSJ is rarely affected by the standoffs when the value is more than 1.25 CD. Therefore, the focus of the following analysis will be mainly on the jet under the 2.0 CD standoff condition.

Table 3. List of computation conditions and results.

Sample	Al (wt.%)	Granule Diameter (μm)	Al Content in HSSJ (wt.%)				
			1.0 CD	1.25 CD	1.5 CD	1.75 CD	2 CD
1	30	40	20.36	20.33	20.08	20.27	20.38
2	30	60	18.80	18.48	17.95	17.53	17.58
3	30	80	13.57	13.23	15.15	16.21	16.23
4	30	100	8.28	7.99	10.84	10.40	11.64

Geometrical morphology of jets formed by granules of different size at 2 CD standoff are shown in Figure 12. By comparison, smaller granules are more easily dispersed in the jet formed by the reactive material liner. When the granule size is $40 \mu\text{m}$, the aluminum particle can enter the tip area of the jet, while the $100 \mu\text{m}$ situation has no particles entering the jet tip. Thus, the dispersion of the particles in the jets increases as the granule size decreases. This effect is related to the different velocities of the granules, as explained in the next sections.

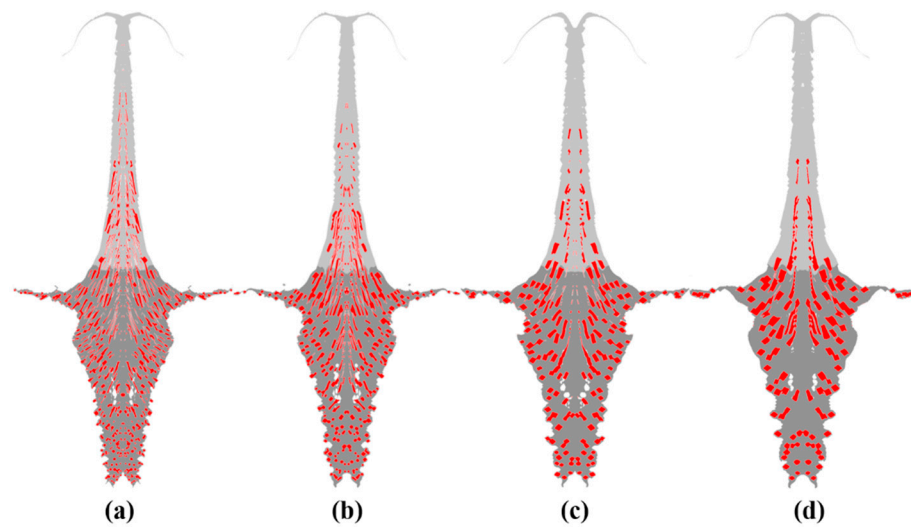


Figure 12. Geometrical morphology of jets formed by Al granules of different average size at 2 CD standoff: (a) $\Phi_{Al} = 40 \mu\text{m}$, (b) $\Phi_{Al} = 60 \mu\text{m}$, (c) $\Phi_{Al} = 80 \mu\text{m}$ and (d) $\Phi_{Al} = 100 \mu\text{m}$.

In order to describe the change of aluminum content in each part of the jet, the following Equation (9) is proposed to calculate the relative aluminum content Δ_{AL} [13]:

$$\Delta_{AL} = \frac{m_{AL} - m_{0,AL}}{m_{0,AL}} \times 100\% \quad (9)$$

where m_{AL} is the aluminum mass fraction in the corresponding part of jet, $m_{0,AL}$ is the initial aluminum mass fraction in the reactive material liner.

In Figure 13, the reactive material jets of different granule diameters are equidistantly divided into 10 parts (the same division method as Figure 10) and the relative aluminum content Δ_{AL} distribution in each part of the cases is shown for each granule size. The plot shows that, as a whole, the aluminum content in the reactive material jet increases at first and then decreases from the head to the tail independently of the granule size. For the four defined granule sizes, there is a maximum Al content in the middle region (parts 4–6) of the jet, increasing with the granule size. On the contrary, for the upper region of the jet (parts 7–10), the Al content decreases and it is lower for the larger granule size condition.

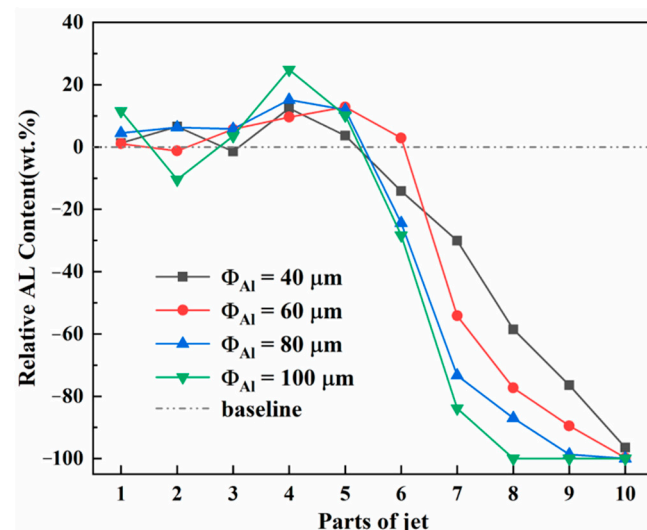


Figure 13. Relative Al content in each part of jet at 2 CD standoff. Note: The parts are defined using the same division method as Figure 10; the baseline corresponds to the original aluminum content in the liner.

The above results indicate that, in the jet formation process, smaller particles are more likely to enter the front part of the jet (the part with higher velocity), leading to a higher aluminum content in the head of the jet, which is consistent with the particle distribution characteristic in HSSJ in the table above. This is due to the fact that under the same loading condition, larger particles gain lower velocity compared with smaller particles, making it more easily to generate relative displacement. Assuming that the load on aluminum particles in the jet formation process is in a single direction and is proportional to the projection area of the particles, the acceleration of aluminum particles can be calculated by:

$$a_{granule} = \frac{3q}{4\rho r} \quad (10)$$

where q is the stress per unit area, ρ is the granule density, and r is the granule diameter. The product (ρr) is related to mass, therefore the size and mass of granule have the same dependence. Meanwhile, the mass and acceleration are related inversely. Accordingly, the acceleration of the particle is inversely proportional to the granule diameter, and finally results in a higher velocity of the smaller granule. Figure 14 shows the aluminum particle velocity and the velocity difference ($V_{PTFE} - V_{AL}$) profiles over time. The Al particle velocity curves show that the aluminum particles in all cases first accelerate integrally, then decelerate for a period of time, and finally accelerate again. At the same time, larger particles decelerate more than the smaller ones, and finally lead to the increase of the average velocity difference among the four kinds of particles. It should be noted that, in order to show the real speed difference, all the average velocities at each moment in Figure 14 only calculate material with velocities higher than 0 m/s. Additionally, after 8 μ s, the material in the middle and bottom of the liner is accelerated and calculated into the average velocity of aluminum particles, resulting in a decline section in the velocity curve. Therefore, the deceleration corresponding to the granule size actually reflects its acceleration ability. The velocity difference curves in the Figure 14 show that, velocity difference increases with the particle diameter, leading to larger relative displacement between the two components. Finally, the content of aluminum granules in the HSSJ decreases while the content of aluminum granules in the slug increases.

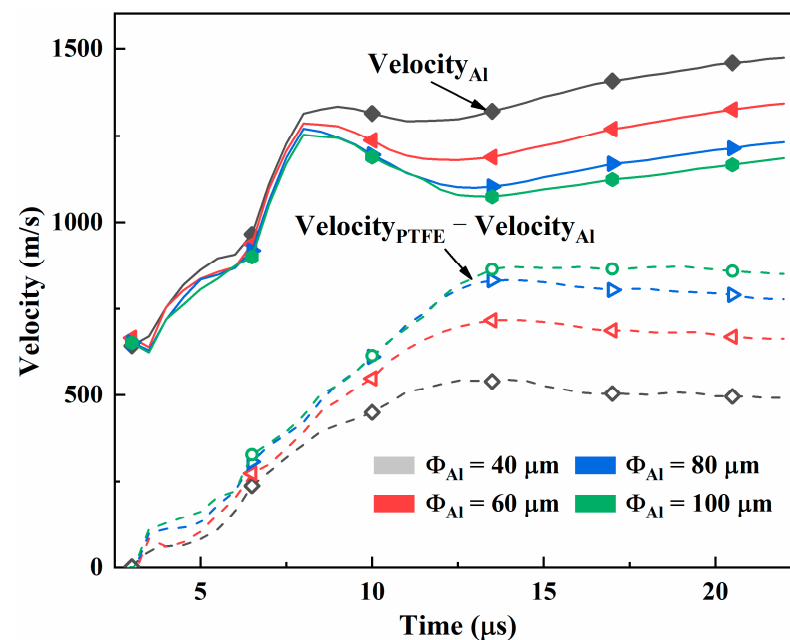


Figure 14. Velocity–time profiles of Al and PTFE-Al. Note: All the average velocities at each moment only calculate material with velocities higher than 0 m/s.

The result suggests that because of its weaker speed-up-ability, larger granules would have a higher proportion of particles which concentrate in the middle and bottom area of the jet. On the contrary, smaller particles accelerate faster and can disperse more into the HSSJ. Therefore, the smaller Al particles could be used in the engineering design to increase the density of the jet head which leads to a higher penetration performance. However, a previous study [10] showed that smaller Al particles speed up the reaction of the reactive material resulting in a weaker penetration performance. Thus, the diameter of the Al particles should be controlled within a relatively appropriate range to obtain a more balanced penetration performance and reaction capacity.

3.4. Evolution of Granules from Liner to Jet

The influence of the initial particle distribution in the liner on the particle distribution characteristics of the jet is studied in this section. A uniform distribution of discrete model is conducted and the reactive material liner is divided into three parts from top to bottom. Figure 15 shows the movement of the particles from different parts of the liner. Firstly, the particles from the top parts of the liner move to the symmetry axis, and the PTFE matrix accelerates faster than the Al particles due to its lower density. The PTFE then gathers into the jet ahead of the Al particles at $6 \mu\text{s}$. With the collapse of the liner and the elongation of the jet, the particles from the top part of the liner are distributed to the head and tail of the jet, and the particles from the middle and bottom section move to the head and neck of the jet.

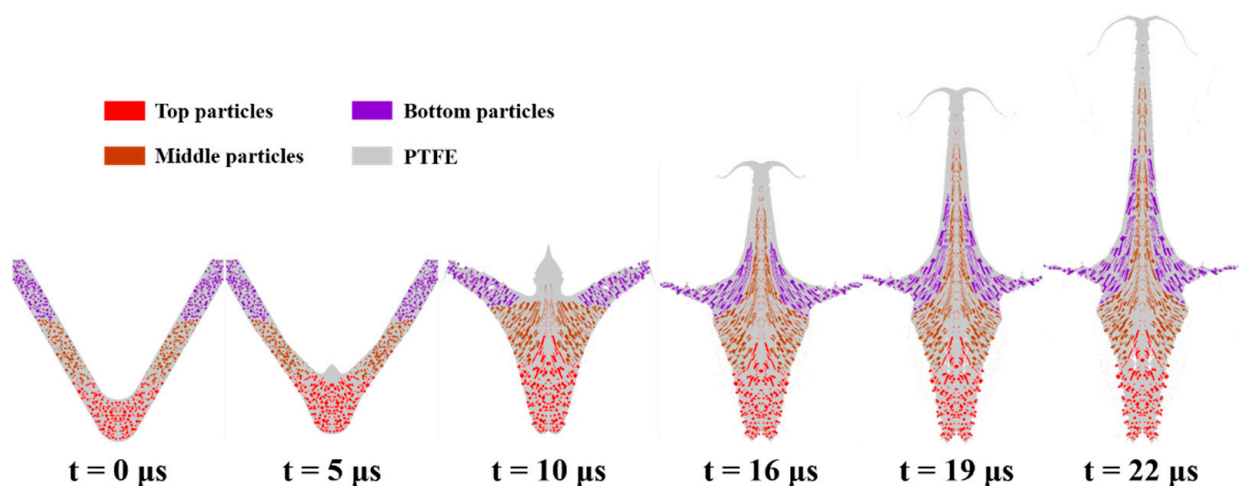


Figure 15. Typical uniform-distributed particles movement in the jet formation process.

The mass fraction and velocity charts of the aluminum particles from different parts of the liner are shown in Figure 16. In Figure 16a, the jet formed by the liner with uniform distributed particles is divided into 10 parts, and the mass fractions of the particles from each part are shown as three curves, respectively. As a whole, the particles from three parts of the liner are distributed in sequence from the head to the slug. The bottom particles are mainly distributed in the top and middle area of the jet, and the top particles are mainly distributed in the slug. In HSSJ, most of the aluminum particles are from the bottom and the middle area of the liner, while the top particles can hardly enter the HSSJ. Figure 16b shows the velocity–time profile of the Al particles from three parts of the liner. The figure shows that, in the formation process, the top particles are first accelerated, and then quickly drop to a relatively low speed. The middle and bottom particles are subsequently accelerated to a higher speed. At the same time, both the curves of the middle and the top particles contain a deceleration period. That is because when the wall of the liner collapses and closes, pressure is transferred from the back forward to the particles closer to the axis, and forcing them into the area with higher velocity. As a result, the particles from other areas

slow down. As the jet continues elongating, this energy transfer gradually decreases and the velocity of the middle and top particles tends to be stable.

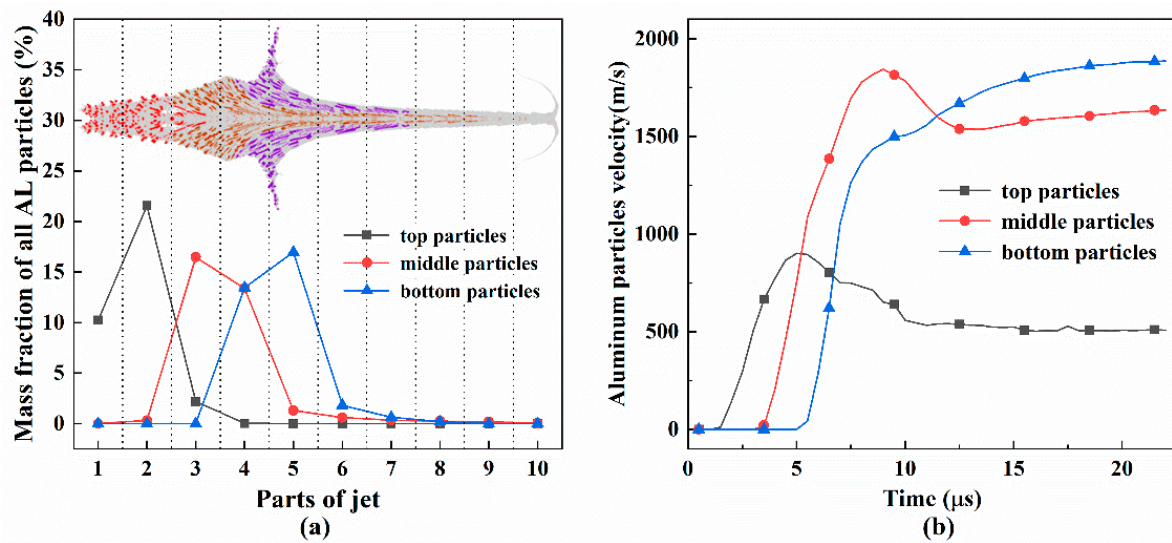


Figure 16. Velocity and mass fraction of Al particles from different parts: (a) mass distribution of Al particles from different parts along the jet axis at 2 CD standoff; (b) average velocity of Al particles from different parts.

3.5. Granule Distribution Induced Jet Particle Distribution

According to the above result, the particles from the middle and the bottom part of the liner have a significant impact on the density of the HSSJ. Besides, the powder-pressed manufacturing process also causes uneven density of each part of the reactive material liner, which is due to the concentration effect of the particles [22,23]. Figure 17 shows the liner models of different particle distributions. Four liner models with uneven particle distribution (Figure 17a,b,d,e) are studied and compared with the uniform density one (Figure 17c). All the liner models are equally divided by area into three parts, and each part is filled with different quantities of Al particles until the overall aluminum particle mass in the liner is m , so that all the cases have the same Al particle mass fraction ($w_{\text{Al}} = 30\%$) in the liner. Besides, the Al particle diameter in all samples is set as $40 \mu\text{m}$. At the same time, the particle distribution characteristic of each sample is represented by $\rho_{\text{liner}} = m_{\text{top}}/m_{\text{bottom}}$, where the middle region of the liners maintains the same concentration in all cases. The five models correspond to configurations with maximum granulate concentration in the bottom region ($\rho_{\text{liner}} = 0.5$), up to the top region ($\rho_{\text{liner}} = 2$).

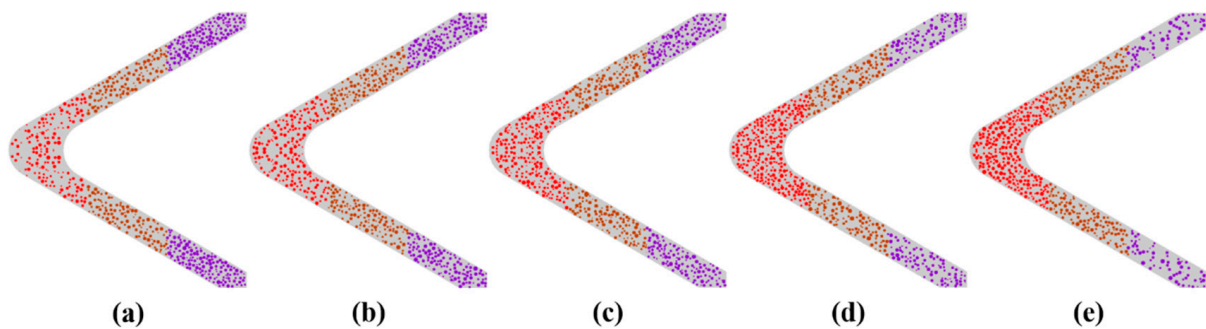


Figure 17. Liner models of different particle distributions: (a) $\rho_{\text{liner}} = 0.5$, (b) $\rho_{\text{liner}} = 0.75$, (c) $\rho_{\text{liner}} = 1$, (d) $\rho_{\text{liner}} = 1.5$ and (e) $\rho_{\text{liner}} = 2$. Note: The material colors are the same as in Figure 15.

The aluminum mass ratio in HSSJ for different liner granule distributions are shown in Table 4. Figure 18 shows the typical images of 2 CD-standoff jet with different initial particle distribution. In all the cases in Figure 18, the top particles are mainly distributed in the slug, the middle particles are mainly distributed in the back and middle of the jet, and the bottom particles are distributed in the front of the jet. The simulations show clearly that the middle and bottom particles are the main components of aluminum particles in the HSSJ.

Table 4. Al content in HSSJ for different liner granule distributions according to ρ_{liner} .

Sample	ρ_{liner}	Initial Al Content (wt.%)			Al Content in HSSJ (wt.%)		
		Top	Middle	Bottom	Top	Middle	Bottom
1	0.5	22.22	33.33	44.44	0	25.17	74.83
2	0.75	28.57	33.33	38.10	0.19	25.99	73.82
3	1	33.33	33.33	33.33	0.33	29.44	70.23
4	1.5	40	33.33	26.67	0.53	35.96	63.51
5	2	44.44	33.33	22.22	3.57	51.70	44.73

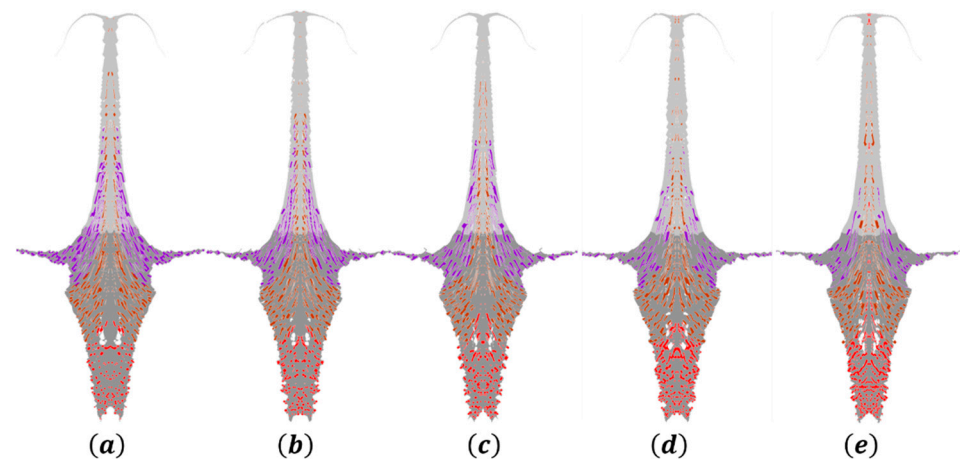


Figure 18. Typical images of 2 CD-standoff jet with different initial particle distribution: (a) $\rho_{liner} = 0.5$, (b) $\rho_{liner} = 0.75$, (c) $\rho_{liner} = 1$, (d) $\rho_{liner} = 1.5$ and (e) $\rho_{liner} = 2$. Note: The particle colors are the same as in Figure 15. The light gray corresponds to HSSJ while the dark gray corresponds to slug.

Table 4 shows the mass ratio of the particles from different parts of liner to all aluminum material in HSSJ. The results show that with the increase of ρ_{liner} (top particles content in liner increases, bottom particles content in liner decreases), the content of bottom particles in HSSJ decreases while the content of the middle particles increases. However, there is a small increase of the content of top particles in HSSJ. As shown in Figure 18e, the top particles are only distributed in the tip of the jet (the red material) in HSSJ. That is because only a small portion of the top particles which is close to the jet axis can flow into the tip in the formation process. The increase of the portion of the middle particles is due to the decrease of the bottom particle content since the top particles can rarely enter the HSSJ. Besides, the mass ratio of the middle and bottom particles in HSSJ is still above 95%, which means the middle and bottom particles are the key components of the Al in HSSJ. However, in general, the bottom particle density has the greatest influence on the Al particle content in HSSJ.

Figure 19 shows the relative Al content in each part of the jet of different samples. The illustration shows that, with the increase of the ρ_{liner} , the position where the maximum relative Al content appears in each sample moves from the middle area to the tail. In the tip of the jet (parts 9 and 10), the sample with more initial particles in the top area of the

liner gains more relative aluminum content. That is because the content of the top particles in HSSJ rises with the quantity of the initial top particles in the liner. In the middle parts (parts 4–8), the relative aluminum content in the jet of each sample decreases successively with the increase of ρ_{liner} . This is because the bottom particles are mainly distributed in the middle part of the jet, therefore more particles are distributed in the middle part of the jet with the increase of the quantity of the initial bottom particles. On the contrary, the relative aluminum content in the jet of the samples decreases successively with the increase of ρ_{liner} in the slug (parts 9 and 10). This is because the top particles are mainly distributed in the slug. As the quantity of particles in the top area of the liner increases, more particles are distributed in the slug.

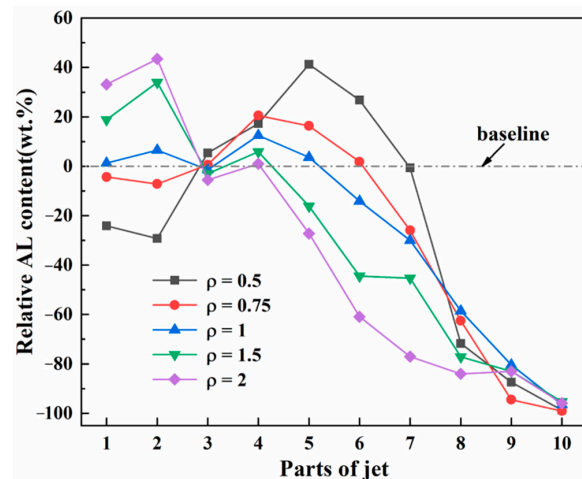


Figure 19. Relative Al content in each part of jet.

The change of the Al particle distribution characteristics in the jet with the initial particle distribution in the liner is qualitatively discussed above. It should be noted that, on the premise that the overall Al quantity in the liner remains unchanged, the aluminum content in the HSSJ should be related to the ρ_{liner} , which is the ratio of the particle quantity in the top area to that in the bottom area of the liner. Assuming that the relationship between the two can be expressed by $wt_{AL} = k \times \rho_{liner} + b$. The fitted curve according to the simulation data is shown in Figure 20, and the constant k and b are fitted as -10.01 and 28.57 , respectively. For the fitted curve, it shows a downward trend with the increasing of ρ_{liner} .

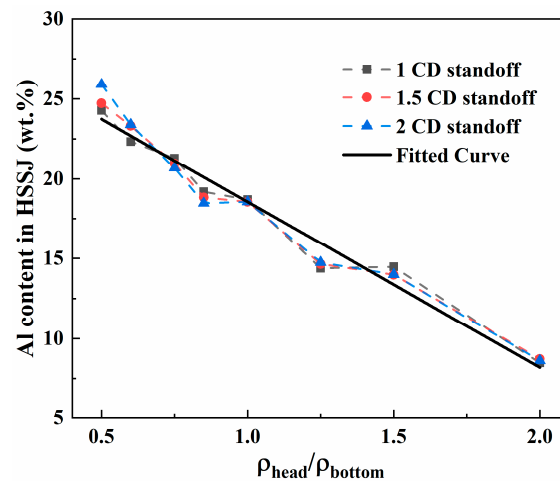


Figure 20. Fitted curve of the Al content in HSSJ of different initial particle distribution in liner.

4. Conclusions

In this paper, a trans-scale discretization method for analyzing the formation of reactive material shaped charge jet is proposed. Additionally, an X-ray experiment is conducted to confirm the validity of the trans-scale numerical simulations. Formation process of PTFE/Al reactive material jet, Al granule size difference induced particle dispersion, and granule distribution induced jet particle distribution are obtained and discussed. The main conclusions are as follows:

- (a) Due to the difference of densities, the PTFE matrix accelerates faster than the Al particles under shock loading. The relative displacement results in a density gradient along the axis of the jet and PTFE becomes the main component of the jet.
- (b) Because of the weaker speed-up-ability, larger Al particles would mainly concentrate in the middle and bottom area of the jet. On the contrary, smaller particles accelerate faster and mainly disperse in the high-speed section of the jet.
- (c) The initial granule distribution in the liner has great influence on the particle distribution in the jet. The particle quantity in the top area of the liner has little impact on the Al content in the HSSJ, while the particles from the middle and bottom area of the liner influence that significantly. Furthermore, the aluminum content in the HSSJ is inversely proportional to the ratio of the particle quantity in the top area to that in the bottom area of the liner.

Author Contributions: G.L., conceptualization, investigation, writing—original draft, writing—review and editing; C.G., conceptualization, writing—original draft; Z.L., resources, conceptualization; L.T., investigation; H.W., conceptualization, writing—review and editing. All authors have read and agreed to the published version of the manuscript.

Funding: This research is supported by the Natural Science Foundation of Beijing, China (No. 1214022).

Institutional Review Board Statement: Not applicable.

Informed Consent Statement: Not applicable.

Data Availability Statement: Not applicable.

Conflicts of Interest: The authors declare no conflict of interest.

References

1. Ames, R. Vented Chamber Calorimetry for Impact-Initiated Energetic Materials. In Proceedings of the 43rd AIAA Aerospace Sciences Meeting and Exhibit, Reno, NV, USA, 10–13 January 2005.
2. Wang, L.; Liu, J.; Li, S.; Zhang, X. Investigation on reaction energy, mechanical behavior and impact insensitivity of W-PTFE-Al composites with different W percentage. *Mater. Des.* **2016**, *92*, 397–404. [[CrossRef](#)]
3. Xu, F.Y.; Yu, Q.B.; Zheng, Y.F.; Lei, M.A.; Wang, H.F. Damage effects of double-spaced aluminum plates by reactive material projectile impact. *Int. J. Impact Eng.* **2017**, *104*, 13–20. [[CrossRef](#)]
4. Xiao, J.; Zhang, X.; Wang, Y.; Xu, F.; Wang, H. Demolition Mechanism and Behavior of Shaped Charge with Reactive Liner. *Propellants Explos. Pyrotech.* **2016**, *41*, 612–617. [[CrossRef](#)]
5. Wang, Y.; Yu, Q.; Zheng, Y.; Wang, H. Formation and Penetration of Jets by Shaped Charges with Reactive Material Liners. *Propellants Explos. Pyrotech.* **2016**, *41*, 618–622. [[CrossRef](#)]
6. Guo, H.; Zheng, Y.; Yu, Q.; Ge, C.; Wang, H. Penetration behavior of reactive liner shaped charge jet impacting thick steel plates. *Int. J. Impact Eng.* **2019**, *126*, 76–84. [[CrossRef](#)]
7. Zheng, Y.; Su, C.; Guo, H.; Yu, Q.; Wang, H. Behind-Target Rupturing Effects of Sandwich-like Plates by Reactive Liner Shaped Charge Jet. *Propellants Explos. Pyrotech.* **2019**, *44*, 1400–1409. [[CrossRef](#)]
8. Xiao, J.; Zhang, X.; Guo, Z.; Wang, H. Enhanced Damage Effects of Multi-Layered Concrete Target Produced by Reactive Materials Liner. *Propellants Explos. Pyrotech.* **2018**, *43*, 955–961. [[CrossRef](#)]
9. Zheng, Y.; Su, C.; Guo, H.; Yu, Q.B.; Wang, H.F. Chain damage effects of multi-spaced plates by reactive jet impact. *Def. Technol.* **2021**, *17*, 393–404. [[CrossRef](#)]
10. Wang, H.F.; Guo, H.G.; Geng, B.Q.; Yu, Q.; Zheng, Y. Application of reactive materials to double-layered liner shaped charge for enhanced damage to thick steel target. *Materials* **2019**, *12*, 2768. [[CrossRef](#)] [[PubMed](#)]
11. Su, C.H.; Wang, H.F.; Xie, J.W.; Ge, C.; Zheng, Y.F. Penetration and damage effects of reactive material jet against concrete target. *Acta Armament.* **2019**, *40*, 1829–1835.

12. Austin, R.A.; Mcdowell, D.L.; Benson, D.J. Mesoscale simulation of shock wave propagation in discrete Ni/Al powder mixtures. *J. Appl. Phys.* **2012**, *111*, 123511. [[CrossRef](#)]
13. Wagner, F.; Ouarem, A.; Gu, C.F.; Allain-Bonasso, N.; Toth, L.S. A new method to determine plastic deformation at the grain scale. *Mater. Charact.* **2014**, *92*, 106–117. [[CrossRef](#)]
14. Ge, C.; Dong, Y.X.; Maimaituersun, W. Microscale Simulation on Mechanical Properties of Al/PTFE Composite Based on Real Microstructures. *Materials* **2016**, *9*, 590. [[CrossRef](#)] [[PubMed](#)]
15. Qiao, L.; Zhang, X.F.; He, Y.; Shi, A.S.; Guan, Z.W. Mesoscale simulation on the shock compression behaviour of Al-W-Binder granular metal mixtures. *Mater. Des.* **2013**, *47*, 341–349. [[CrossRef](#)]
16. Wang, F.; Ma, D.; Wang, P.; Liu, J.; Jiang, J. Experimental and numerical study on the meso-scope characteristics of metal composites jets by a shaped charge. *J. Appl. Phys.* **2019**, *126*, 095901. [[CrossRef](#)]
17. Wang, F.; Jiang, J.W.; Men, J.B. Mesoscopic Numerical Simulation on the Formation of Tungsten-Copper Shaped Charge Jet. *Acta Armament.* **2018**, *39*, 245–253.
18. Tang, L.; Ge, C.; Guo, H.G.; Yu, Q.B.; Wang, H.F. Force chains based mesoscale simulation on the dynamic response of Al-PTFE granular composites. *Def. Technol.* **2021**, *17*, 56–63. [[CrossRef](#)]
19. Tang, L.; Wang, H.; Lu, G.; Zhang, H.; Ge, C. Mesoscale study on the shock response and initiation behavior of Al-PTFE granular composites. *Mater. Des.* **2021**, *200*, 109446. [[CrossRef](#)]
20. Guo, H.; Xie, J.; Wang, H.; Yu, Q.; Zheng, Y. Penetration Behavior of High-Density Reactive Material Liner Shaped Charge. *Materials* **2019**, *12*, 3486. [[CrossRef](#)] [[PubMed](#)]
21. Century Dynamics, Inc. *AUTODYN Theory Manual (Revision 4.3)*; ANSYS Inc.: Canonsburg, PA, USA, 2005.
22. Zhao, Z.Y. *Research of Penetration Properties and Penetration Mechanism of W-Cu Alloy Shaped Charge Liner*; Beijing Institute of Technology: Beijing, China, 2016.
23. Sippel, T.R.; Son, S.F.; Groven, L.J. Aluminum agglomeration reduction in a composite propellant using tailored Al/PTFE particles. *Combust. Flame* **2014**, *161*, 311–321. [[CrossRef](#)]